Research Square

Preprints are preliminary reports that have not undergone peer review.
They should not be considered conclusive, used to inform clinical practice,
or referenced by the media as validated information.

Enhancement of photocurrent in NdCoO 3 via the plasmonic effect of silver microparticles

Carlos R. Michel

carlos.muribe@academicos.udg.mx

Universidad de Guadalajara

Alma H. Martínez-Preciado

Universidad de Guadalajara

Research Article

Keywords: Ag/NdCoO3, Microwave-assisted combustion, UV Photosensor, Plasmonic effect

Posted Date: November 5th, 2026

DOI: https://doi.org/10.21203/rs.3.rs-11243489/v1

License: This work is licensed under a Creative Commons Attribution 4.0 International License.
Read Full License

Additional Declarations: No competing interests reported.

Enhancement of photocurrent in $NdCoO_3$ via the plasmonic effect of silver microparticles

Carlos R. Michel [1,*] and Alma H. Martínez-Preciado [2]

[1] Universidad de Guadalajara, Centro Universitario de Ciencias Exactas e Ingenierías, Departamento de Física, Marcelino G. Barragán 1421, Guadalajara 44430, Jalisco, México

[2] Universidad de Guadalajara, Centro Universitario de Ciencias Exactas e Ingenierías, Departamento de Ingeniería Química, Blvd. Marcelino G. Barragán 1421, Guadalajara 44430, Jalisco, México

* Correspondence:

Carlos R. Michel

Email: carlos.muribe@academicos.udg.mx

Tel.: +52 33 38 14 37 06

ORCID: 0000-0002-3955-1825

Alma H. Martínez-Preciado

ORCID: 0000-0002-9765-9316

Abstract

Rare earth cobalt perovskites of formula $ReCoO_3$ are an important group of materials that have applications in many emerging technologies such as energy storage devices, photocatalysis, gas sensors, and many more. An effective strategy for improving their physical and physicochemical properties has been the formation of metal-semiconductor heterojunctions. In this work, the effect of adding silver microparticles (Ag (μPs)) to $NdCoO_3$ on its photodetection properties was investigated. For the preparation of $NdCoO_3$ and $Ag/NdCoO_3$, the microwave-assisted combustion method was used, which provides a fast, inexpensive and efficient route to synthesize them, without subsequent high temperature calcination. The photoconductive properties in UV light were evaluated through photocurrent (I_{ph}) measurements, at room temperature, on thick films made with the as-prepared materials. The results revealed an increase of at least one order of magnitude in the variation of I_{ph} (ΔI_{ph}) in $Ag/NdCoO_3$, compared with the single-phase material. This was attributed to the plasmonic effect produced by the homogeneous distribution of Ag (μPs) in the perovskite. Polarization curves confirmed the quantitative detection of this radiation. For near-infrared radiation (NIR), no significant response was obtained for $NdCoO_3$; however, reliable results were registered in $Ag/NdCoO_3$. Based on the results, it was possible to conclude that the introduction of non-agglomerated Ag (μPs) into cobalt-based perovskites represents a suitable method for improving their photosensing properties.

Keywords: $Ag/NdCoO_3$; Microwave-assisted combustion; UV Photosensor; Plasmonic effect

1. Introduction

Perovskite-type oxides of formula ABO_3 have remarkable properties in areas like catalysis, superconductivity, ferroelectrics, photovoltaics, energy storage, and many more [1]. Particularly, lanthanide cobalt perovskites ($ReCoO_3$, where Re is a rare-earth) have attracted interest since the early 1970s due to the possible application of $La_{1-x}Sr_xCoO_3$ ($x \leq 0.5$) as a substitute for platinum in automotive catalytic converters to reduce pollutant emissions [2-6]. In photocatalysis, some of these materials exhibit performance similar to that of TiO_2 (anatase and rutile phases) for the degradation of polluting organic dyes such as methyl orange and methylene blue [7, 8]. Cobalt-based perovskites have also been the subject of active research in the field of electrocatalysis to improve oxygen and hydrogen evolution reactions, which are employed in energy conversion devices and solid oxide fuel cells [9, 10]. In gas sensors, they display high response and selectivity to environmental gases due to the remarkable adsorption properties [11]. Although the photosensing response of some cobalt perovskites has been investigated, the majority remain unexplored; $NdCoO_3$ is a notable example [12, 13]. Time ago, this oxide was investigated as a catalyst for methane oxidation, where the results revealed better performance than those obtained from $LaCoO_3$ and $PrCoO_3$ [14]. $NdCoO_3$ has also been tested as a photocatalyst for the degradation of anionic and cationic organic dyes, like phenol red and methyl violet, with promising results [15]. For gas sensing applications, it has been investigated for detecting CO and acetone, while its electrical, thermoelectric, and thermochromic properties have also been reported [16-24].

Various methods have been used for the preparation of this perovskite, such as

coprecipitation, solid-state reaction, the sol-gel method, thermal decomposition of salts, and molten salts, among others. Table 1 shows a summary of the main characteristics of them and those of the resulting materials [14-29]. As can be observed, $NdCoO_3$ can adopt a cubic or orthorhombic crystal structure; soft chemistry routes, such as coprecipitation and the sol-gel method, produce cubic nanoparticles at relatively low temperatures, whereas methods based on solid-state reaction and molten salts primarily generate micrometer-sized orthorhombic particles [30].

Although there is abundant information regarding the synthesis of $NdCoO_3$, little is available on the preparation of metal-semiconductor heterojunctions formed by this material and noble metals, or on the resulting physical properties. Given that the optical bandgap energy (E_g) of $NdCoO_3$ (2.84 eV) is narrower than that of common UV photosensor materials like ZnO or TiO_2, it would be possible to detect this radiation as well as radiation of lower energy [31, 32]. Therefore, the effect of incorporating silver particles into this material on its optoelectronic properties is the main objective of this study. To prepare $NdCoO_3$ and $Ag/NdCoO_3$, the use of a direct, fast and energy-saving method was explored. In addition, the thermoelectric properties of both materials were evaluated for comparative purposes.

2. Experimental

$NdCoO_3$ was synthesized by the microwave-assisted combustion method by dissolving 2 g of $Nd(NO_3)_3 \cdot 6H_2O$ (99.9%, Alfa-Aesar) and 1.32 g of $Co(NO_3)_2 \cdot 6H_2O$ (99%, J.T. Baker), in 20 mL of an aqueous solution containing 0.1 g polyvinyl alcohol (PVA). PVA was used to promote an

exothermic reaction with the nitrates under microwave irradiation (MW), which was applied through a domestic microwave oven operating at a frequency of 2.45 GHz and a power of 500 W. Once the precursor dried, MW continued to be applied intermittently for 30 min until its full combustion. Due to the high temperature achieved in this process, the resulting material was not subsequently calcined. For the preparation of Ag/ $NdCoO_3$, 0.1 g of $AgNO_3$ (99.9%, J.T. Baker) was added to the solution of neodymium and cobalt nitrates. The subsequent steps followed the order already mentioned.

The crystal structure of the synthesized materials was analyzed by X-ray powder diffraction (XRD), at room temperature, using an Empyrean (PANalytical) diffractometer, which operates with monochromatic Cu $K_{\alpha 1}$ radiation. The surface morphology was examined by field emission scanning electron microscopy (FESEM), using a Jeol microscope (JSM-IT 710HR). *In situ*, surface chemical analyses were performed with an X-ray energy dispersive spectrometer (EDS) attached to the microscope. The chemical composition of samples was also analyzed by X-ray photoelectron spectroscopy (XPS), using a Specs Phoibos 150 spectrometer, operated with monochromatic Al K_{α} radiation (1486.61 eV). Absorbance measurements were performed using a Thermo Scientific UV-vis spectrophotometer (Helios Zeta).

The photocurrent characterization was carried out on thick films made with the as-prepared $NdCoO_3$ and $Ag/NdCoO_3$ powders. The latter were sonicated in anhydrous ethyl alcohol and immediately deposited with a syringe into a ceramic ring of 5 mm diameter. The latter was fixed to an alumina substrate by silver wires, which act as electrodes. To improve the electrical

conductivity and mechanical strength, the films were annealed at 300°C, for 5 h. Next, to protect them from contamination and moisture, they were placed in sealed, transparent fused silica tubes; Fig. 1 shows a schematic of the experimental setup. The light sources used in these tests were LEDs of nominal wavelength 365 nm (UV-A) and 843 nm (NIR). The optical irradiance (E_e) of them was adjusted by a DC power supply (GW, model GPR-1810HD) and measured with a Thorlabs optical power meter (PM 100D). The photocurrent measurements were performed in DC mode using an Agilent 34401A digital multimeter in series with a DC power supply and collecting data with a PC. *I-V* curves were acquired under similar light conditions, using a potentiostat (Solartron 1285), interfaced to a PC. Thermoelectrical measurements were performed on the same films placing them in a temperature-programmable muffle-type furnace (Thermolyne 48000). The heating rate used in these experiments was 100°C/h.

3. Results and Discussion

3.1 Crystal structure and chemical composition of samples

The microwave-assisted combustion method provides an efficient, direct and inexpensive route to synthesize diverse ceramic materials [33-36]. It consists of the controlled exothermic reaction occurring when metal nitrates and organic compounds, used as a fuel, are exposed to MW irradiation. The high thermal energy generated by this process is frequently enough to crystallize the target compounds. Fig. 2 shows typical XRD patterns collected from $NdCoO_3$ and $Ag/NdCoO_3$ samples, without subsequent calcination. $NdCoO_3$ crystallized in the cubic structure, with a lattice

parameter a = 7.546 Å and space group Pm3m, and was identified using the JCPDF file No. 025-1064. In the case of Ag/$NdCoO_3$, metallic silver was identified by XRD lines located at 2θ = 38.1° (planes (111)), 44.3° (200), and 64.4° (220), using the JCPDF file No. 01-089-3722, while $NdCoO_3$ retained the same crystal structure. As previously mentioned, $NdCoO_3$ can also crystallize in an orthorhombic structure; however, the perovskite-type structure is preserved in both cases, since the Goldschmidt tolerance factor (*t*) lies between 0.8 and 0.9 [37]. This factor is defined as:

$$t = \frac{r_A + r_O}{\sqrt{2}\,(r_B + r_O)} \quad (1)$$

Where r_A, r_B and r_O are the ionic radii of the elements in the perovskite: $r_A = Nd^{3+}$ (1.109 Å), $r_B = Co^{3+}$ (0.61 - 0.63 Å), and $r_O = O^{2-}$ (1.4 Å). According to the literature, nanostructured materials exhibit a significant number of crystalline defects (oxygen vacancies) that lead to oxygen non-stoichiometry, resulting in a mixed-valence state for the cobalt ions Co^{3+} and Co^{2+} (r_B: 0.72 - 0.75 Å), a situation frequently observed in many cobalt-based perovskites.

On the other hand, the average crystallite size (*D*) was calculated from the XRD data, using the Scherrer equation:

$$D = \frac{\kappa\lambda}{\beta cos\theta} \quad (2)$$

Where the shape factor is κ (0.9), λ corresponds to the X-ray wavelength (1.5406 Å), β is the full width at half maximum (FWHM) of each XRD peak, and θ corresponds to the Bragg angle. The calculations gave *D* = 32 nm for single-phase $NdCoO_3$, 32.8 nm for silver-doped $NdCoO_3$, and 23 nm for silver particles.

3.2 Surface morphology and chemical composition

Fig. 3(a) shows the morphology of a sample of $NdCoO_3$, which has an internal porous core with large irregularly shaped cavities, more than 10 μm in size, while the exterior shows a smooth and dense surface. The large internal porosity was formed by the emission of gases, mainly CO_2 and NO_x, during thermal decomposition of organic matter (PVA) and nitrates, caused by microwave irradiation. At high magnification, Fig. 3(b) shows a detailed view of the external shell, which exhibits a dense agglomeration of sintered microparticles (μPs) of size above 150 nm. This microstructure reveals the high temperature spontaneously achieved by the strong exothermic reaction promoted by MW radiation on nitrates and PVA, which occurs under controlled conditions. On the other hand, Fig. 3(c) shows a typical EDS spectrum of this sample, where characteristic X-ray emissions of Nd, Co, O, C and Au of energies below 20 keV can be noticed. The gold emission was produced by the thin layer deposited by plasma sputtering to improve image resolution. Meanwhile the carbon signal was caused by the colloidal paint used to fix the powder in the sample holder. The energy of neodymium orbitals detected by this technique can be observed at 5.23 ($L_{\alpha 1}$), 5.2 ($L_{\alpha 2}$), 5.72 ($L_{\beta 1}$), 6.09 ($L_{\beta 2}$), 6.6 ($L_{\gamma 1}$), and 0.97 keV ($M_{\alpha 1}$). For cobalt, the peaks are located at: 6.93 ($K_{\alpha 1}$), 6.91 ($K_{\alpha 2}$), and 7.65 keV ($K_{\beta 1}$), while oxygen shows only one emission at 0.52 keV ($K_{\alpha 1}$). These results reveal that samples were free of contaminants.

For $Ag/NdCoO_3$, Fig. 4(a) shows a FESEM image acquired at low magnification, where morphological characteristics like those previously observed in the single-phase perovskite can be noticed. At larger magnifications, Fig. 4(b) shows bright dots, indicated by arrows, corresponding

to silver microparticles (Ag μPs), which have sizes in the range of 0.12 to 0.3 μm, without visible coalescence among them. Fig. 4(c) shows an EDS spectrum of this sample, where in addition to the elements mentioned above, silver peaks corresponding to energies of 2.98 ($L_{\alpha 1}$), 3.15 ($L_{\beta 1}$), and 3.34 keV ($L_{\beta 2}$) can be noted. Furthermore, Fig. 4(d) shows a FESEM image and a sequence of images corresponding to EDS chemical mapping collected from Nd, Co and Ag. In the case of Nd and Co, a coincidence in their spatial distribution is observed, indicating that both signals are generated by the same material ($NdCoO_3$). In contrast, the bright regions of the FESEM image are associated with the Ag microparticles and form metal-semiconductor heterojunctions with the perovskite.

The chemical composition was also characterized by XPS; Fig. 5(a) shows a wide-scan spectrum obtained from an $NdCoO_3$ sample, in which peaks emitted by neodymium, cobalt, and oxygen can be observed. For neodymium, Fig. 5(b) shows a narrow scan acquired around the $3d_{3/2}$ and $3d_{5/2}$ emissions, which have binding energies of 980.7 and 1002.9 eV, respectively. These values were verified with those reported in the literature and show good agreement [38]. The satellite peak centered at 1008 eV can be attributed to spin-orbit interactions from Nd-Co bonds. For cobalt ions, Fig. 5(c) displays $2p_{1/2}$ and $2p_{3/2}$ peaks, centered at 794.3 and 779 eV, respectively. The presence of a satellite peak centered at ~783.5 eV is an indication of high spin Co^{2+} ions, which, in combination with the two peaks already mentioned, associated with high spin Co^{3+}, allow us to conclude that cobalt ions are in a mixed valence state [29, 39, 40]. Furthermore, Fig. 5(d) shows the 1s peak of oxygen, located at ~527.8 eV, which is associated with the formation of Nd-

O and Co-O bonds. In this graph, a large peak centered at 529.5 eV can be attributed to oxygen vacancies. As mentioned before, this kind of lattice defect is characteristic of nanostructured perovskite-type oxides. It is worth noting that Hu et al. obtained a similar oxygen XPS profile from a nanostructured $NdCoO_3$ sample with orthorhombic structure, suggesting that, at the nanoscale, oxygen vacancies form independently of the crystal structure [29].

Regarding the XPS analyses of $Ag/NdCoO_3$, Fig. 6(a) shows a typical wide scan exhibiting features like those shown in Fig. 5(a). In addition, low-intensity emissions corresponding to 3d levels of silver, at approximately 370 eV, can be also observed in this spectrum. For neodymium, Fig. 6(b) displays no significant differences compared with Fig. 5(b), where the slight variations are within the margin of error of the instrument. Something similar occurs with the narrow spectrum of cobalt 2p levels, where a detailed inspection reveals no relevant changes. For the oxygen signal, Fig. 6(d) shows a similar peak overlapping than that observed in $NdCoO_3$; however, a decrease in the intensity of the peak located at 530.17 eV can indicate a variation in oxygen vacancies. The narrow spectrum acquired around $3d_{3/2}$ and $3d_{5/2}$ peaks of silver particles can be observed in Fig. 6(e), which is consistent with what has been reported in the literature [38]. This result confirms that silver does not form oxides or any other compound during synthesis, nor does it intercalate into the $NdCoO_3$ structure.

3.3 Optical bandgap energy of $NdCoO_3$ and $Ag/NdCoO_3$

The optical bandgap energy of $NdCoO_3$ and $Ag/NdCoO_3$ was determined from absorbance

data using the Tauc method. For this purpose, each powder was ground in an agate mortar and sonicated in deionized water before measurement. Fig. 7 shows typical $(\alpha h\nu)^2$ *vs.* $h\nu$ graphs obtained from these materials, where α is the absorption coefficient, h the Planck´s constant, ν the light frequency, and $h\nu$ the photon energy. The point where each arrow intersects the x-axis indicates an E_g value of 3.2 eV for $NdCoO_3$, which is slightly higher than that reported by Kianipour et al. (2.84 eV) [15]. In the case of $Ag/NdCoO_3$, the calculated E_g was 2.95 eV; however, it could not be compared because as far as we know it has not been reported in a prior investigation. The bandgap narrowing observed in $Ag/NdCoO_3$ can be attributed to the plasmonic effect of randomly distributed metal-semiconductor heterojunctions. This narrowing had previously been observed in dye-sensitized solar cells based on TiO_2 decorated with gold NPs [41].

3.4 Photocurrent properties of $NdCoO_3$ and $Ag/NdCoO_3$ in ultraviolet light

Photosensors for the ultraviolet region are important to quantify human exposure to this radiation for preventing skin cancer, cataracts, macular degeneration, and eye cancer, among other health issues. They also play a fundamental role in military defense by detecting rockets, missiles, and similar artifacts, which, due to their high kinetic energy, emit radiation in this part of the electromagnetic spectrum. In chromatography, photodiode array detectors are used to quantify organic compounds dissolved in drinking water and other liquids. Then, research in UV photosensor materials and device development is relevant for advanced optoelectronic technologies. On the other hand, the process for detecting specific radiation is carried out by

measuring variations in a physical property of a material, such as electrical conductivity, when it is exposed to various experimental conditions. Common photosensor materials are ZnO, Si, SiC, diamond, GaN, and ZnSe, among others, while several strategies have been investigated for improving their performance. Some of them are based on the deposition of micro or nanoparticles of a noble metal, the fabrication of *p-n* thin films, or a combination of both methods, to cite a few examples [42-46]. Given that the first approach can be easily developed and constitutes a direct and cost-effective method, it was explored in this study.

Fig. 8(a) shows a series of graphs recorded during the exposure of $NdCoO_3$ to several on/off cycles of UV illumination, at room temperature. Each one was obtained using a constant optical irradiance (E_e) in the range 2 - 8 mW/cm^2, applying a bias voltage of 1 V. The results show a sharp increase in photocurrent (I_{ph}) during the first seconds of illumination, with a nearly symmetric decrease in the absence of light. The variation of photocurrent ($\Delta I_{ph} = I_{light} - I_{dark}$) increased from 0.35 μA to 1.73 μA, when E_e increased in the selected range, while the baseline current increased from 1.25 to 1.64 μA. In addition to a rapid variation of I_{ph}, the response pattern was uniform and reproducible over many on/off periods. The common explanation of this phenomenon consists in the formation of electron-hole pairs in the semiconductor, caused by its interaction with photons of a certain energy, which can be expressed by Eq. No. 3:

$$h\nu \rightarrow h^+ + e^- \quad (3)$$

However, a significant amount of that energy is absorbed by the material as heat, which generates phonons, with a simultaneous increase of electrical conductivity [47]. Furthermore,

exciton formation in $NdCoO_3$ is highly probable, given the absorption of light energy and the relatively low responsivity values shown later. Furthermore, regardless of the optical irradiance, in the absence of an applied voltage, charge carrier recombination occurs, resulting in zero photocurrent.

On the other hand, Fig. 8(b) shows graphs of I_{ph} vs. t recorded in $Ag/NdCoO_3$, using the same experimental parameters as in $NdCoO_3$. In this case, an increase in I_{ph} of approximately one order of magnitude can be noticed, having a similar uniform response pattern. It can also be observed that the baseline current increased accordingly, resulting in ΔI_{ph} values ranging from 2.8 μA to 8.9 μA. The proposed energy diagram for this material is shown in Fig. 8(c). Since the work function of silver (Φ_m), which is between 4.17 and 4.74 eV, is smaller than that of $NdCoO_3$ (Φ_s = 4.83 eV), a large electron flow from Ag μPs to the oxide takes place [47-49]. This occurs due to silver has a high density of free electrons (5.86×10^{28} m^3) with a high mobility (5.6×10^{-3} $m^2/V{\cdot}s$), making this element an attractive option for metal-semiconductor heterojunctions [50]. Furthermore, the interaction of UV light with Ag μPs promotes the collective oscillation of electrons, which acquire higher energies, and are known as hot electrons. These electrons overcome the Schottky barrier, which is indicated in Fig. 8(c) as Φ_b ($\Phi_b = \Phi_m - \chi_s$), where χ_s is the electron affinity. The photocurrent generated in this way is further enhanced by localized surface plasmon resonances, which undergo radiative or non-radiative relaxation, where the latter generates high-energy electron-hole pairs [51, 52]. It is worth mentioning that the size, shape and distribution of metallic particles attached to the semiconductor plays a key role in the photocurrent

improvement. In this regard, Sakar el at. reported that random Au NPs deposited on TiO_2 registered the highest current density, when exposed to UV light of 365 nm, compared to those obtained from this oxide having aligned Au slabs on its surface [53].

On the other hand, the responsivity (R_s) of $NdCoO_3$ and $Ag/NdCoO_3$ films in UV light was determined according to Eq. 3 [54].

$$R_s = \frac{\Delta I_{ph}}{(A_{eff})(E_e)} \quad (3)$$

Where ΔI_{ph} was calculated from the graphs shown in Figs. 9(a) and 9(b), respectively, A_{eff} is the effective area of the film ($(\pi)(0.0025\ m)^2$), and E_e was in the range of 2 to 12 mW/cm^2. For comparative purposes, these units were converted to W/m^2, Table 2 shows the corresponding results. For $NdCoO_3$, R_s increased steadily from 12.4 $\times 10^{-4}$ to 50 $\times 10^{-4}$ A/W, while for $Ag/NdCoO_3$ varied from 77.6 $\times 10^{-4}$ to 109 $\times 10^{-4}$ A/W, without following a specific trend. The latter suggests that the formation of metal-semiconductor heterojunctions in this perovskite generates larger and more stable photocurrents, practically independent of E_e.

On the other hand, the variation of photocurrent with applied voltage was investigated through polarization curves while the material was exposed to UV light of E_e values ranging from 1 to 10 mW/cm^2. Figs. 10(a) and 10(b) show I_{ph} - V graphs obtained from $NdCoO_3$ and $Ag/NdCoO_3$, respectively. For $NdCoO_3$, a nearly linear variation of photocurrent with voltage is observed, which increased from 5 to 21 μA, at +5 V. The left side of this figure shows an analogue trend for I_{ph} at negative voltages. In the case of $Ag/NdCoO_3$ the behavior was non-linear, at both positive and

negative voltages, with I_{ph} increasing from 50 to 250 μA at +5 V. This represents an approximate 10-fold increase from that measured for $NdCoO_3$. The non-linear variation of I_{ph} measured in $Ag/NdCoO_3$ can be attributed to Schottky barriers, as mentioned above, and its high values are mainly associated with the generation of hot electrons. Furthermore, when comparing the results recorded at +1 V in Figs. 10(a) and (b), with those shown in the graphs above, a good agreement can be observed; however, the application of higher voltages improves the resolution of light detection.

3.5 Detection of near infrared (NIR) radiation

The detection of NIR radiation (λ = 843 nm) by $NdCoO_3$ was evaluated at various optical irradiances, under a bias voltage of 1 V; however, no significant variation of I_{ph} was registered in multiple on/off cycles. This can be explained by the large difference between the E_g of the perovskite (3.2 eV) and the average energy of the incoming photons (1.47 eV), making the jump of charge carriers from the valence to the conduction band unlikely. Conversely, Fig. 11 shows a typical I_{ph} *vs*. *t* graph recorded in $Ag/NdCoO_3$, using an E_g of 10 mW/cm^2 and 1 V of applied voltage. In this case, an I_{ph} of ~2.2 μA was measured, which represents a great difference compared to the silver-free material. This result indicates that, in addition to the enhanced UV detection performance of $Ag/NdCoO_3$, the absorption bandwidth was broadened through the plasmonic effect, enabling the detection of low-energy radiation. The bandwidth widening by the plasmonic effect has also been of great importance in photovoltaic cells; for example, Sung et al. have

reported a significant improvement in the power conversion efficiency (PCE) of solar cells, resulting from the plasmonic absorption band broadening produced by gold nanorods in ZnO [55]. Analogously, Wu et al. found that silver NPs of irregular shape improve the PCE of perovskite solar cells by the broad-band enhanced plasmonic effect [56]. Furthermore, with a similar objective, Li and coworker proposed for infrared photodetectors an array of gold nanostructures deposited on n-type Si substrates operating by the plasmonic effect [57].

3.6 Thermoelectric properties

To determine the effect of temperature on the electrical conductivity of $NdCoO_3$ and $Ag/NdCoO_3$, measurements were carried out from 320 to 670 K, in the absence of light; Fig. 12(a) shows the corresponding plots obtained with a DC voltage of +0.5 V. This voltage was lower than that used in previous photocurrent characterization due to the high current values registered at high temperature. The graphs show that both materials have a similar behavior, with a strong dependence of σ with T, characteristic of semiconductors [47]. These results are partially consistent with those published by Dudnikov et al., who measured σ in the 300 - 800 K range; however, the changes in slope appearing in each graph of Fig. 12(a), at approximately 350 and 620 K, are not observed in their results [24]. According to Thornton et al. the inflection points observed in σ *vs*. T plots of $NdCoO_3$ reflect the transition from semiconducting behavior at low-temperature to metallic conductivity, observed above 600 K [19]. This behavior is a characteristic of many

rare-earth cobalt perovskites. Subsequently, Capon et al. confirmed these results in $NdCoO_3$ thin films prepared via magnetron sputtering [25].

For Ag/$NdCoO_3$ a slight improvement in σ can be observed at low temperatures, confirming the difference in the dark currents of previous photocurrent results. However, this difference virtually disappears at high temperatures, indicating a marginal effect of silver doping, and where the semiconducting properties of $NdCoO_3$ predominate. It is worth mentioning that the applied voltage plays a key role in this characterization, Fig. 12(b) shows σ *vs*. *T* graphs recorded at +0.5V (already shown in Fig. 12(a)) and that recorded at +0.1 V. In the latter, a significant decrease of σ is observed in the entire temperature range being more pronounced at low temperatures.

Conclusions

Rare-earth cobalt perovskites possess unique electrical and optoelectronic properties that, in many cases, surpass those of perovskites containing iron, chromium, nickel, or other transition metals. Regarding the rare-earth element contained in cobalt-based perovskites, Dudnikov et al. have found that the conductivity follows the next order: $\sigma_{Nd} > \sigma_{Sm} > \sigma_{Gd} > \sigma_{Tb} > \sigma_{Dy}$, making $NdCoO_3$ an interesting and relatively unexplored option for photosensing applications. To improve these properties, a cost-effective and convenient strategy consisting in decorating its surface with Ag μPs was investigated. Among the noble metals, silver possesses important characteristics, such as the highest electrical conductivity, low price, and can be easily incorporated into the host perovskite without oxidizing during the synthesis process. The strong exothermic reaction between

the metal nitrates and organic media when exposed to microwave radiation was used in this work to synthesize the target compounds. This process provides a fast and direct route to prepare many ceramic materials, without intermediate calcination steps. The structural and chemical characterization revealed that materials were well crystallized and free of impurities or secondary phases. On the other hand, the photocurrent measurements performed on $NdCoO_3$ show a large sensitivity to UV light, which significantly increases for $Ag/NdCoO_3$ due to hot electron plasmonic effect. Polarization curves confirm the quantitative detection of UV light, which can be improved by increasing the applied bias voltage. Finally, NIR radiation detection was achieved solely with $Ag/NdCoO_3$, due to the widening of the detectable wavelength range resulting from plasmonic effect.

Acknowledgments

This work was supported by the General Academic Coordination of the Universidad de Guadalajara (U de G), through the PRO-SNI 2026 program.

Author contributions

Conception and design of study: C.R.M. Data acquisition: C.R.M., A.H.M.P., Analysis and interpretation of data: C.R.M., A.H.M.P., Drafting the manuscript: C.R.M., Revising the manuscript critically for important intellectual content: C.R.M., A.H.M.P., Approval of final version for publication: C.R.M. and A.H.M.P.

Funding

Financial support from the General Academic Coordination of the Universidad de Guadalajara, México, through the PRO-SNI 2025 program, is greatly appreciated.

Data availability

The datasets generated during and/or analyzed during the current study are available from the corresponding author on reasonable request.

Declarations

Ethics approval

Not applicable.

Consent to participate

Not applicable.

Clinical trials

In this work, no clinical trials were performed

Consent for publication

Not applicable.

Competing interests

The authors declare not to have conflicts of interest about the publication of this work.

Dual publication

The results/data/figures in this manuscript have not been published elsewhere, nor they are under

consideration for publication.

Authorship

The corresponding author and coauthor have read the journal policies and are submitting this manuscript in accordance with those policies.

References

[1] M.A. Peña, J.L.G. Fierro, Chemical structures and performance of perovskite oxides, Chem. Rev. 101 (2001) 1981−2017.

[2] B. Raveau, M. Seikh, Cobalt Oxides. From Crystal Chemistry to Physics, Wiley-VCH, Weinheim, 2012.

[3] W.F. Libby, Promising catalyst for auto exhaust, Science 171 (1970) 499−500.

[4] R.J.H. Voorhoeve, J.P. Remeika, P.E. Freeland, B.T. Matthias, Rare-earth oxides of manganese and cobalt rival platinum for the treatment of carbon monoxide in auto exhaust, Science 177 (1972) 353−354.

[5] C.H. Kim, G. Qi, K. Dahlberg, W. Li, Strontium-doped perovskites rival platinum catalysts for treating NO_x in simulated diesel exhaust, Science 327 (2010) 1624−1627.

[6] S. Royer, D. Duprez, F. Can, X. Courtois, C. Batiot-Dupeyrat, S. Laassiri, H. Alamdari, Perovskites as substitutes of noble metals for heterogeneous catalysis: dream or reality, Chem. Rev. 114 (2014) 6556−6564.

[7] W. Wang, M.O. Tadé, Z. Shao, Research progress of perovskite materials in photocatalysis- and photovoltaics-related energy conversion and environmental treatment, Chem. Soc. Rev. 44 (2015) 5371−5408.

[8] M. Humayun, Z. Li, M. Israr, A. Khan, W. Luo, Ch. Wang**,** Z. Shao**,** Perovskite type ABO_3 oxides in photocatalysis, electrocatalysis, and solid oxide fuel cells: state of the art and future prospects, Chem. Rev. 125 (2025) 3165–3241.

[9] T. Long, D. Song, Y. Zhou, X. Yu, X. Wang, C. Li, H. Chen, G. Li, F. He, Modulating activity of lattice oxygen of ABO_3 perovskite oxides in redox reactions: a review, ACS Appl. Mater. Interfaces, 17 (2025) 20590−20612.

[10] J. Simböck, M. Ghiasi, S. Schönebaum, U. Simon, F.M.F. de Groot, R. Palkovits, Electronic parameters in cobalt-based perovskite-type oxides as descriptors for chemocatalytic reactions, Nature Comm. 11 (2020) 652.

[11] J.C. Ding, H.Y. Li, Z.X. Cai, X.D. Zhang, X. Guo, $LaCoO_3$-based sensors with high sensitivity to carbon monoxide, RSC Adv. 5 (2015) 65668–65673.

[12] H. Liu, B. Guo, K. Zheng, R. Xie, X. Zhang, X. Wu, Y. Zhang, Ch. Li, Novel visible-light-driven photoconductive properties of $LaCoO_3$ epitaxial nano-thin films, Mater. Lett. 20 (2017) 446–449.

[13] C.R. Michel, M.A. Lopez, A.H. Martinez-Preciado, G.G. Carbajal-Arizaga, Novel UV sensing and photocatalytic properties of $DyCoO_3$, J. Sensors (2019) 5682645.

[14] A. Baiker, P.E. Marti, P. Keusch, E. Fritsch, A. Reller, Influence of the A-site cation in $ACoO_3$ (A = La, Pr, Nd, and Gd) perovskite-type oxides on catalytic activity for methane combustion, J. Catal. 146 (1994) 268–276.

[15] S. Kianipour, F.S. Razavi, I. Waleed, S.E. Izzat, I. Farhan, T.S. Hussein, K. Heydaryan, M. Salavati-Niasari, $NdCoO_3$ nanostructures as promising candidate photocatalysts for boosting visible-light-driven photocatalytic degradation of organic pollutants, J. Sci, Adv. Mater. Dev. 7 (2022) 100506.

[16] L. Malavasi, C. Tealdi, G. Flor, G. Chiodelli, V. Cervetto, A. Montenero, M. Borella, $NdCoO_3$ perovskite as possible candidate for CO-sensors: thin films synthesis and sensing properties, Sens. Actuat. B 105 (2005) 407–411.

[17] I.A. Abdel-Latif, M.M. Rahman, S.B. Khan, Neodymium cobalt oxide as a chemical sensor, Results Phys. 8 (2018) 578–583.

[18] E.E. Ateia, M.M. Arman, M. Morsy, Synthesis, characterization of $NdCoO_3$ perovskite and its uses as humidity sensor, Appl. Phys. A 125 (2019) 882–883.

[19] G. Thornton, F.C. Morrison, S. Partington, B.C. Tofield, D.E. Williams, The rare earth cobaltates: localised or collective electron behaviour? J. Phys. C: Solid State Phys. 21 (1988) 2871–2880.

[20] C.G.S. Pillai, A.M. George, High-temperature thermal conductivity of $NdCoO_3$ and $GdCoO_3$, Int. J. Thermophys. 12 (1991) 207-221.

[21] B. Scherrer, A.S. Harvey, S. Tanasescu, F. Teodorescu, A. Botea, K. Conder, A.N. Grundy, J. Martynczuk, L.J. Gauckler, Correlation between electrical properties and thermodynamic stability of $ACoO_{3-\delta}$ perovskites (A = La, Pr, Nd, Sm, Gd), Phys. Rev. B 84 (2011) 085113.

[22] S.V. Kurgan, G.S. Petrov, L.A. Bashkirov, A.I. Klyndyuk, Properties of $Nd_{1-x}Gd_xCoO_3$ solid solutions, Inorg. Mater. 40 (2004) 1224–1228.

[23] H. Hashimoto, T. Kusunose, T. Sekino, Influence of ionic sizes of rare earths on thermoelectric properties of perovskite-type rare earth cobalt oxides $RCoO_3$ (R = Pr, Nd, Tb, Dy), J. Alloy. Compd. 484 (2009) 246–248.

[24] V.A. Dudnikov, A.S. Fedorov, Yu.S. Orlov, L.A. Solovyov, S.N. Vereshchagin, S.Yu. Gavrilkin, A.Yu. Tsvetkov, M.V. Gorev, S.V. Novikov, S.G. Ovchinnikov, Thermoelectric properties of the $SmCoO_3$ and $NdCoO_3$ cobalt oxides, Ceram. Int. 46 (2020) 17987–17991.

[25] F. Capon, A. Boileau, C. Carteret, N. Martin, P. Boulet, J. F. Pierson, Cation size effect on the thermochromic properties of rare earth cobaltites, $RECoO_3$ (RE: La, Nd, Sm), J. Appl. Phys. 114 (2013) 113510.

[26] W. Chen, F. Li, J. Yu, Salt-assisted combustion synthesis of highly dispersed perovskite $NdCoO_3$ nanoparticles, Mater. Lett. 61 (2007) 397–400.

[27] H. Wang, G. Li, L. Li, Molten-salt-mediated synthesis and low-temperature electrical conduction of $LnCoO_3$ (Ln = Pr, Nd, Sm, and Gd), J. Alloy. Compd. 612 (2014) 227–232.

[28] A. Beganskiene, R. Raudonis, A. Kareiva, Sol-gel preparation and characterization of novel mixed-metal cobaltates-aluminates, Chem. Eng. Comm. 200 (2013) 305–315.

[29] Q. Hu, B. Yue, W. Su, D. Yang, Y. Wang, X. Dong, J. Liu, Syntheses, characterization, magnetic, and electrochemical properties of perovskite-type $NdFeO_3$ and $NdCoO_3$ nanofibers, J. Am. Ceram. Soc. 105 (2022) 6732–6743.

[30] V.A. Dudnikov, Y.S. Orlov, L.A. Solovyov, S.N. Vereshchagin, S.Y. Gavrilkin, A.Y. Tsvetkov, D.A. Velikanov, M.V. Gorev, S.V. Novikov, S.G. Ovchinnikov, Effect of multiplicity fluctuation in cobalt ions on crystal structure, magnetic and electrical properties of $NdCoO_3$ and $SmCoO_3$, Molecules, 25 (2020) 1301.

[31] B.D. Boruah, Zinc oxide ultraviolet photodetectors: rapid progress from conventional to self-powered photodetectors, Nanoscale Adv. 1 (2019) 2059–2085.

[32] L. Sang, M. Liao, M. Sumiya, A comprehensive review of semiconductor ultraviolet photodetectors: from thin film to one-dimensional nanostructures, Sensors, 13 (2013) 10482–10518.

[33] S. Chamani, M. Khatamian, N.S. Peighambardoust, U. Aydemir, Microwave-assisted auto-combustion synthesis of binary/ternary Co_xNi_{1-x} ferrite for electrochemical hydrogen and oxygen evolution, ACS Omega 6 (2021) 33024−33032.

[34] G.S. Kumar, R. Srinivasan, G. Karunakaran, E. Kolesnikov, M. Kim, D.Yuasam. Karpenkov, Microwave-assisted combustion synthesis of soft ferromagnetic spinel MFe_2O_4 (M = Ni, Mg, Zn) nanoparticles using *Citrus limon* fruit extract as a fuel, Appl. Phys. A 127 (2021) 546.

[35] R.B. Nuernberg, M.R.Morelli, Synthesis of BSCF perovskites using a microwave-assisted combustion method, Ceram. Int. 42 (2016) 4204−4211.

[36] T. Alammar, I. Hamm, V. Grasmik, M. Wark, A.V. Mudring, Microwave-assisted synthesis of perovskite $SrSnO_3$ nanocrystals in ionic liquids for photocatalytic applications, Inorg. Chem. 56 (2017) 6920−6932.

[37] F.S. Galasso, Perovskites and High T_c Superconductors, Gordon and Breach Sci. Pub. New York, USA, 1990.

[38] J.F. Moulder, W.F. Stickle, P.E. Sobol, K.D. Bomben, Handbook of X-ray Photoelectron Spectroscopy, Perkin-Elmer, Eden Prairie, USA, 1992.

[39] M.C. Biesinger, B.P. Payne, A.P. Grosvenor, L.W.M. Lau, A.R. Gerson, R. St.C. Smart, Resolving surface chemical states in XPS analysis of first row transition metals, oxides and hydroxides: Cr, Mn, Fe, Co and Ni, Appl. Surf. Sci. 257 (2011) 2717–2730.

[40] A. González, E. Martínez-Tamayo, A. Beltrán-Porter, V. Cortés Corberán, Synthesis of high surface area perovskite catalysts by non-conventional routes, Catal. Today, 33 (1997) 361–369.

[41] J. Villanueva-Cab, P. Olalde-Velasco, A. Romero-Contreras, Z. Zhuo, F. Pan, S.E. Rodil, W. Yang, U. Pal, Photocharging and band gap narrowing effects on the performance of plasmonic photoelectrodes in dye-sensitized solar cells, ACS Appl. Mater. Interfaces 10 (2018) 31374−31383.

[42] E. Monroy, F. Omnés, F. Calle, Wide-bandgap semiconductor ultraviolet photodetectors, Semicond. Sci. Technol. 18 (2003) R33–R51.

[43] P. Chinnamuthu, P. Pooja, Metal oxide heterostructures for light detector applications, In: N. Kumar, B.M. Soucase, Eds. Metal Oxide-Based Heterostructures, Elsevier, Amsterdam, 2023, pp. 453–499.

[44] B. Nabet Ed., Photodetectors, Materials, Devices and Applications, Woodhead, Cambridge, UK, 2016.

[45] H. Marouf, N. Abdel-Salam, E.S.M. El-Rabaie, A.N.Z. Rashed, K.M. ElKhamisy, A comprehensive review of photodetectors: materials, enhancement techniques, perspectives, and recent directions, J. Opt. (2025).

[46] G. Yang, J. Li, M. Wu, X. Yu, J. Yu, Recent advances in materials, structures, and applications of flexible photodetectors, Adv. Electron. Mater. 9 (2023) 2300340.

[47] R.H. Bube, Electrons in Solids, 3rd Ed. Academic Press, San Diego, 1992, pp. 159–170.

[48] H.B. Michaelson, The work function of the elements and its periodicity, J. Appl. Phys. 48 (1977) 2729–2733.

[49] Q. Hu, H. Luo, Ch. Song, Y. Wang, B. Yue, J. Liu, Density functional theory insights into conduction mechanisms in perovskite-type $RCoO_3$ nanofibers for future resistive random-access memory applications, Molecules, 29 (2024) 6056.

[50] Ch. Kittel, Introduction to Solid State Physics, 7rth Ed. Wiley, New York, 1996, pp. 148–150.

[51] C. Clavero, Plasmon-induced hot-electron generation at nanoparticle/metal-oxide interfaces for photovoltaic and photocatalytic devices, Nature Photon. 8 (2014) 95–103.

[52] Y. Liu, Q. Chen, D.A. Cullen, Z. Xie, T. Lian, Efficient hot electron transfer from small Au nanoparticles, Nano Lett. 20 (2020) 4322–4329.

[53] S. Sarkar, V. Gupta, T, Tsuda, J, Gour, A, Singh, O. Aftenieva, A.M. Steiner, Ma. Hoffmann, S. Kumar, A. Fery, J. Joseph, T.A.F. König, Plasmonic charge transfers in large-scale metallic and colloidal photonic crystal slabs, Adv. Functional Mater. Interf. 31 (2021) 2011099.

[54] Ch. Scales, P. Berini, Thin-film Schottky barrier photodetector models, IEEE J. Quantum Elect. 46 (2010) 633–643.

[55] Y.-M. Sung, Y.-Ch. Lai, M.-F. Tsai, H.-H. Hsieh, M.-H. Yang, P.P. Wei, Ch.-S. Yeh, F Ch. Hsu, Y.-F. Chen, Broad band plasmonic nanomaterials for high performance solar cells, J. Mater. Chem. C 4 (2016) 513–520.

[56] Y. Wu, X. Sun, S. Dai, M. Li, L. Zheng, Q. Wen, B. Tang, D-.Q. Yun, L. Xiao, Broad-band-enhanced plasmonic perovskite solar cells with irregular silver nanomaterials, ACS Appl. Mater. Interfaces 14 (2022) 16269−16278.

[57] W. Li, J. Valentine, Metamaterial perfect absorber based hot electron photodetection, Nano Lett. 14 (2014) 3510–3514.

Figure captions

Figure 1 Drawing of the experimental setup used for photocurrent measurements.

Figure 2 XRD patterns of $Ag/NdCoO_3$ and $NdCoO_3$ synthesized by the microwave-assisted combustion method.

Figure 3 Microstructure and chemical composition of $NdCoO_3$: (a) and (b) FESEM images obtained at different magnifications, and (c) EDS spectrum.

Figure 4 Morphology of $Ag/NdCoO_3$: (a) Low magnification FESEM photo, (b) Random distribution of Ag μPs, (c) Chemical analysis obtained by EDS, and (d) SEM image of a typical area of the sample and the corresponding mapping of Nd, Co and Ag.

Figure 5 XPS results obtained from $NdCoO_3$: (a) Survey scan, (b) Neodymium $3d_{3/2}$ and $3d_{5/2}$ peaks, (c) Cobalt $2p_{1/2}$ and $2p_{3/2}$, and (d) Oxygen signals.

Figure 6 XPS spectra of $Ag/NdCoO_3$: (a) Wide scan, (b) Nd $3d_{3/2}$ and $3d_{5/2}$, (c) Co $2p_{1/2}$ and $2p_{3/2}$, (d) O 1s, and (e) Ag $3d_{3/2}$ and $3d_{5/2}$ peaks.

Figure 7 Optical bandgap energy of $NdCoO_3$ and $Ag/NdCoO_3$.

Figure 8 I_{ph} *vs. t* graphs obtained from (a) $NdCoO_3$ and (b) $Ag/NdCoO_3$, in UV light at different optical irradiances, and (c) Proposed energy band diagram for $Ag/NdCoO_3$.

Figure 9 Responsivity graphs obtained in UV light from (a) $NdCoO_3$ and (b) $Ag/NdCoO_3$.

Figure 10 I_{ph} vs. V curves acquired from (a) $NdCoO_3$ and (b) $Ag/NdCoO_3$ films in UV light.

Figure 11 NIR response measured in $Ag/NdCoO_3$.

Figure 12 σ *vs*. T graphs acquired from (a) $NdCoO_3$ and $Ag/NdCoO_3$ at 0.5 V, and (b)

$Ag/NdCoO_3$ at 0.1 and 0.5 V.

Table caption

Table 1 Summary of preparation methods and characteristics of the resulting materials.

Table 2 Responsivity calculated at various optical irradiances from 20 to 120 W/m^2 for $NdCoO_3$ and $Ag/NdCoO_3$.

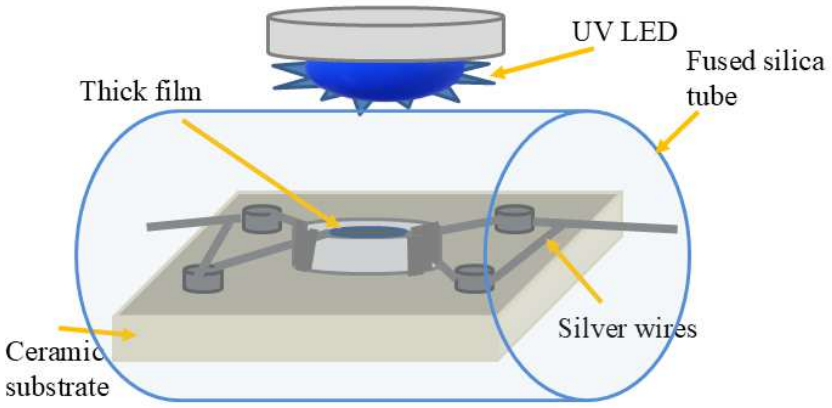

UV LED
Fused silica tube
Thick film
Silver wires
Ceramic substrate

Figure 1

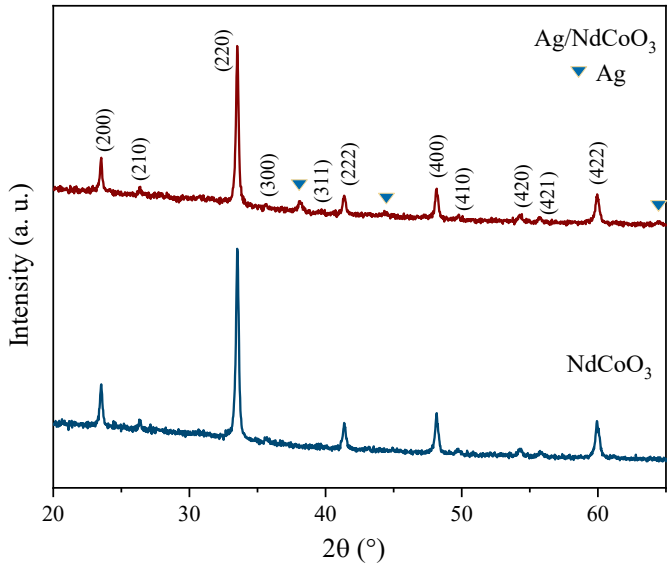

Ag/NdCoO3
Ag
NdCoO3
(200)
(210)
(220)
(300)
(311)
(222)
(400)
(410)
(420)
(421)
(422)
Intensity (a. u.)
2θ (°)
20
30
40
50
60

Figure 2

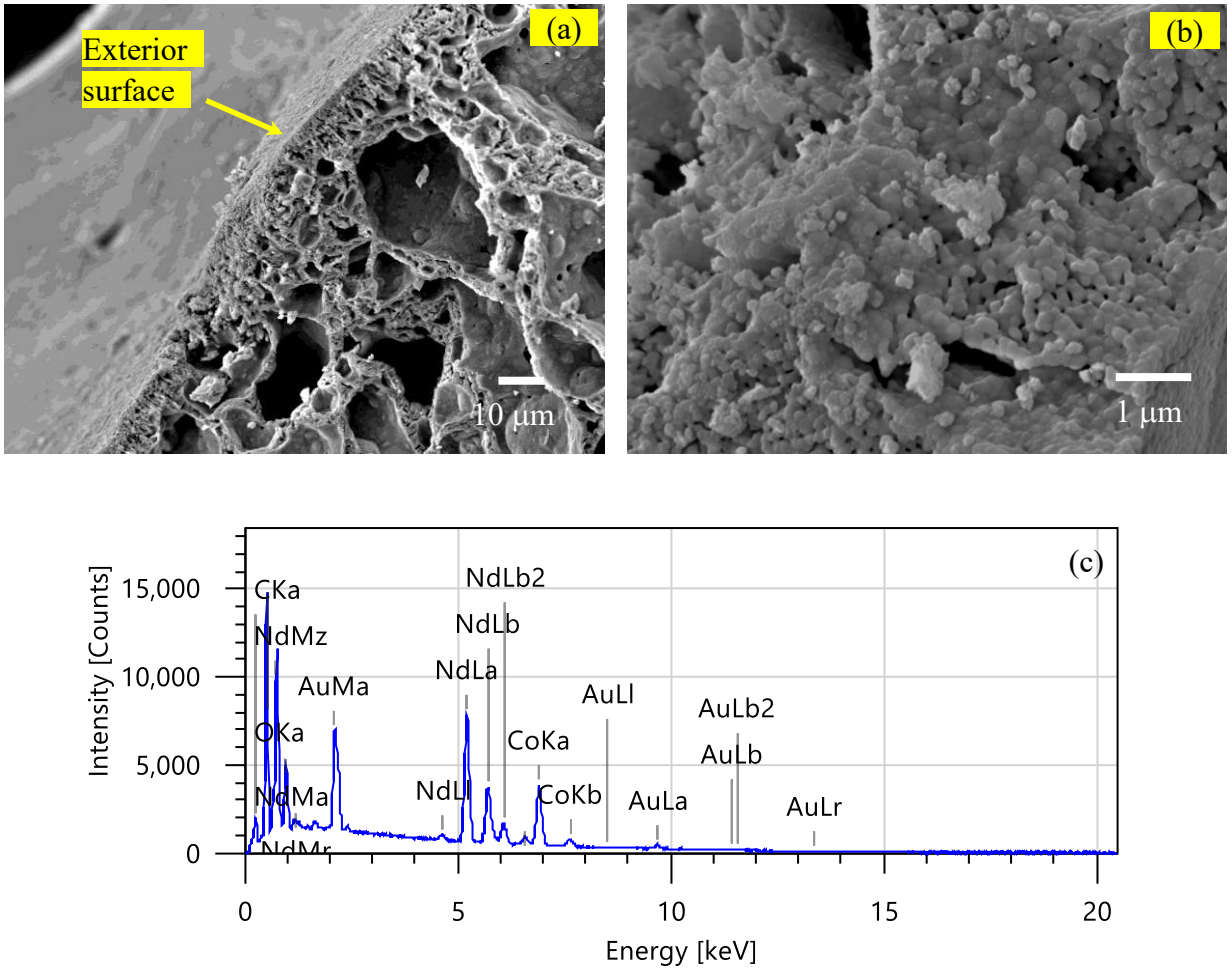

(a)
Exterior surface
10 µm
(b)
1 µm
(c)
Intensity [Counts]
15,000
10,000
5,000
0
CKa
NdMz
AuMa
OKa
NdMa
NdMr
NdLb2
NdLb
NdLa
NdLl
CoKa
CoKb
AuLl
AuLa
AuLb2
AuLb
AuLr
0
5
10
15
20
Energy [keV]

Figure 3

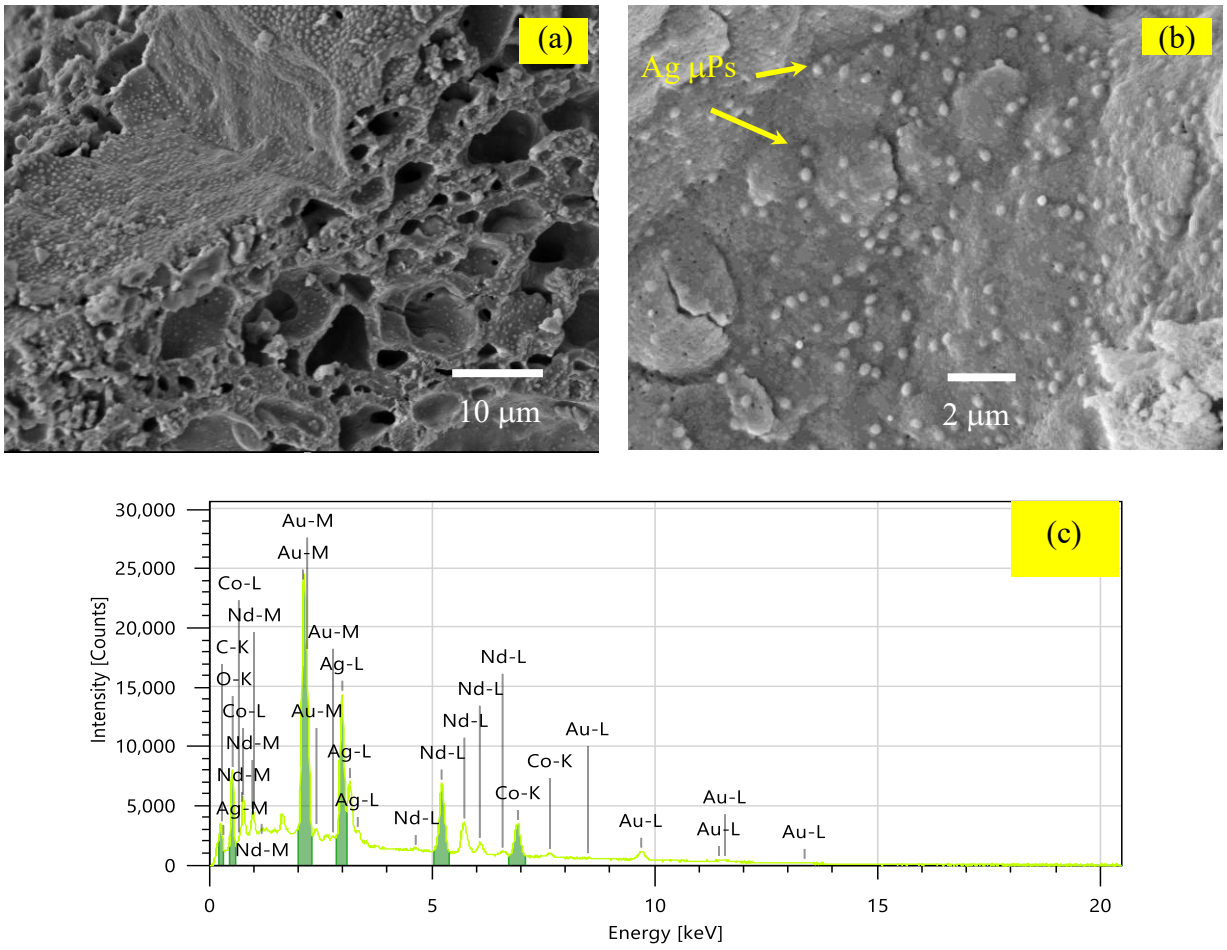

(a)
10 µm
(b)
Ag µPs
2 µm
(c)
Intensity [Counts]
Energy [keV]
Au-M
Co-L
Nd-M
C-K
O-K
Ag-L
Nd-L
Co-K
Au-L
Ag-M
(d)
1 µm
Nd
Co
Ag

Figure 4

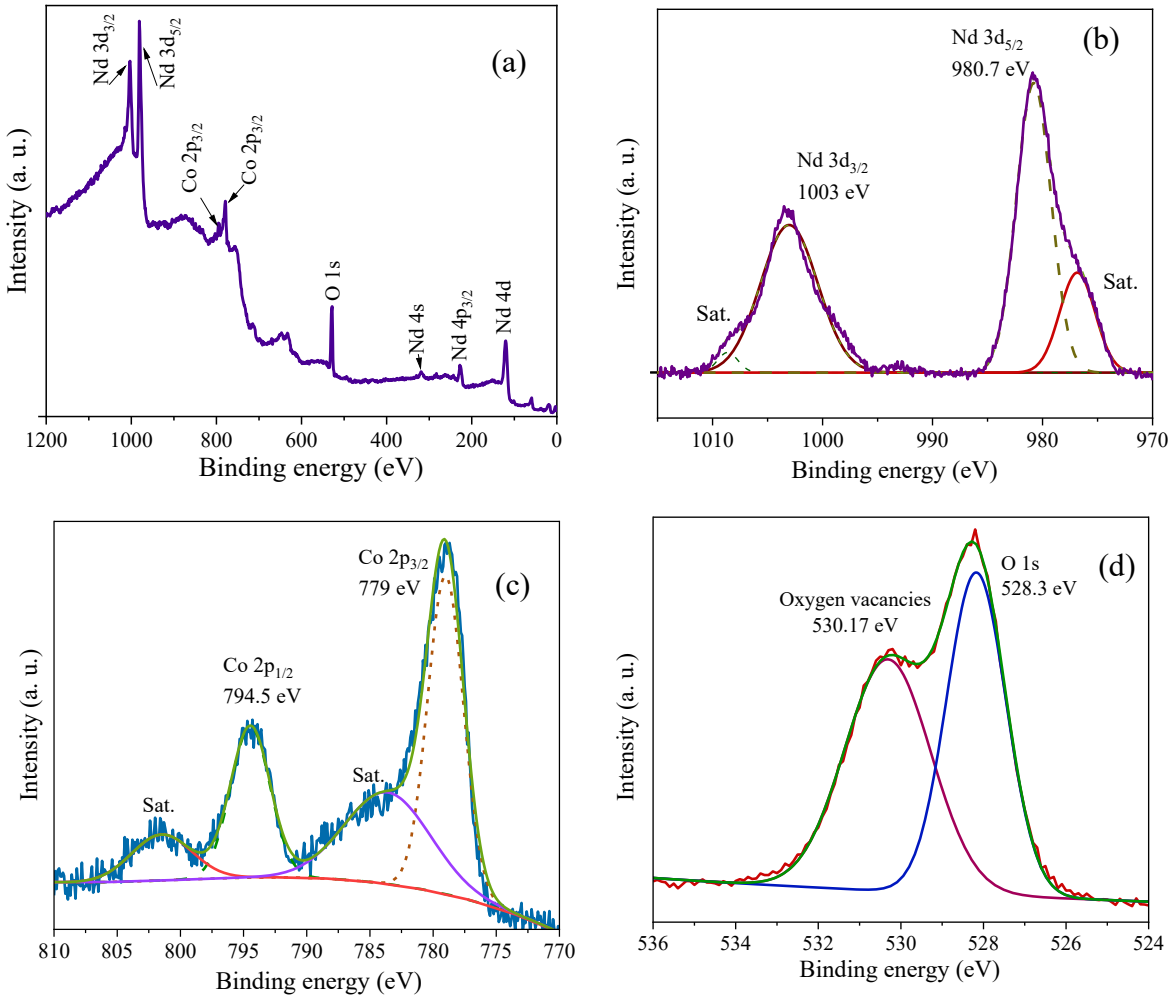

(a)
Nd 3d3/2
Nd 3d5/2
Co 2p3/2
Co 2p3/2
O 1s
Nd 4s
Nd 4p3/2
Nd 4d
Intensity (a. u.)
Binding energy (eV)
(b)
Nd 3d5/2
980.7 eV
Nd 3d3/2
1003 eV
Sat.
Sat.
Intensity (a. u.)
Binding energy (eV)
(c)
Co 2p3/2
779 eV
Co 2p1/2
794.5 eV
Sat.
Sat.
Intensity (a. u.)
Binding energy (eV)
(d)
O 1s
528.3 eV
Oxygen vacancies
530.17 eV
Intensity (a. u.)
Binding energy (eV)

Figure 5

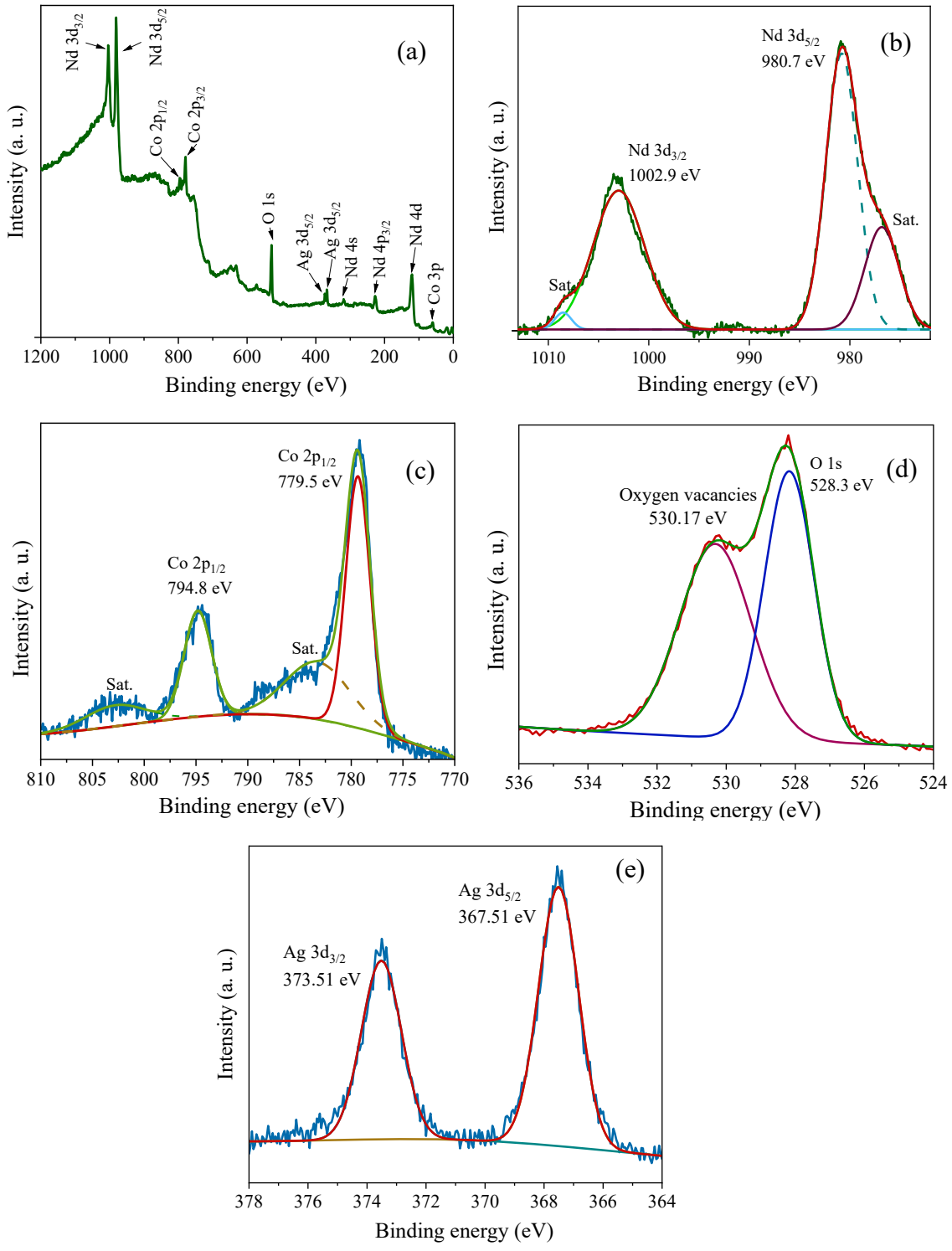

(a)
Nd 3d3/2
Nd 3d5/2
Co 2p1/2
Co 2p3/2
O 1s
Ag 3d5/2
Ag 3d3/2
Nd 4s
Nd 4p3/2
Nd 4d
Co 3p
Intensity (a. u.)
Binding energy (eV)
(b)
Nd 3d5/2
980.7 eV
Nd 3d3/2
1002.9 eV
Sat.
Sat.
(c)
Co 2p1/2
779.5 eV
Co 2p1/2
794.8 eV
Sat.
Sat.
(d)
O 1s
528.3 eV
Oxygen vacancies
530.17 eV
(e)
Ag 3d5/2
367.51 eV
Ag 3d3/2
373.51 eV

Figure 6

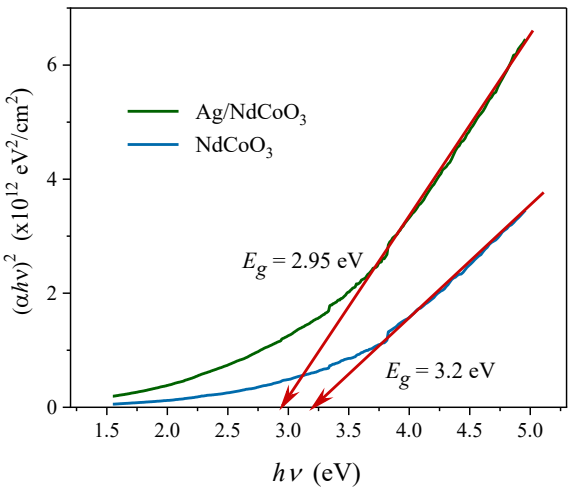
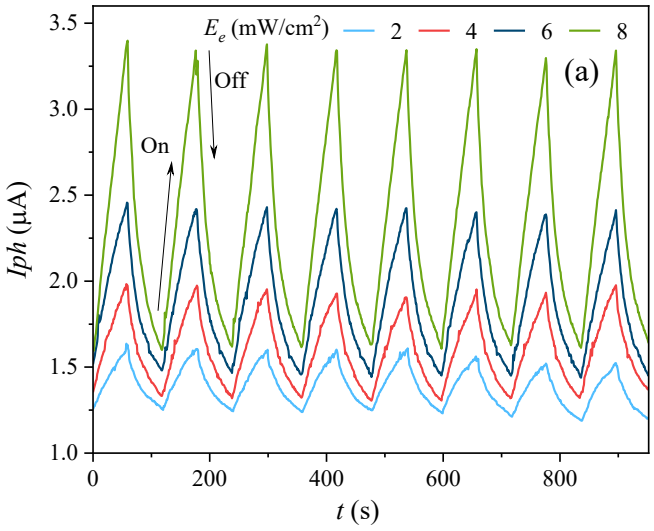
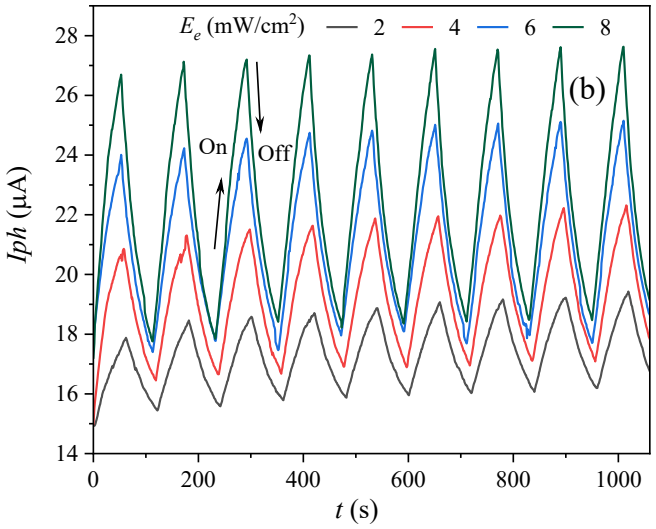

Ag/NdCoO3
NdCoO3
Eg = 2.95 eV
Eg = 3.2 eV
(αhν)2 (x10^12 eV^2/cm^2)
hν (eV)
0
2
4
6
1.5
2.0
2.5
3.0
3.5
4.0
4.5
5.0

Figure 7


E_e (mW/cm^2) 2 4 6 8
(a)
On
Off
Iph (μA)
t (s)


E_e (mW/cm^2) 2 4 6 8
(b)
On
Off
Iph (μA)
t (s)

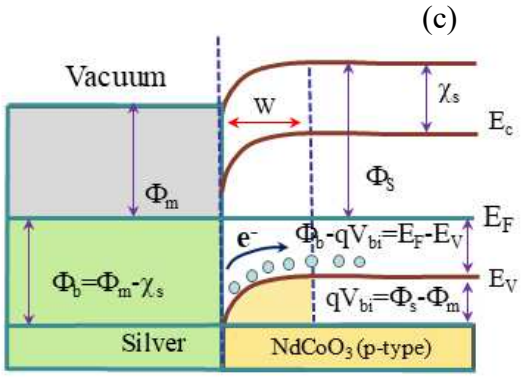

(c)
Vacuum
W
χ_s
E_c
Φ_m
Φ_S
E_F
e$^-$
Φ_b-qV$_{bi}$=E$_F$-E$_V$
Φ_b=Φ_m-χ_s
E$_V$
qV$_{bi}$=Φ_s-Φ_m
Silver
NdCoO$_3$ (p-type)

Figure 8

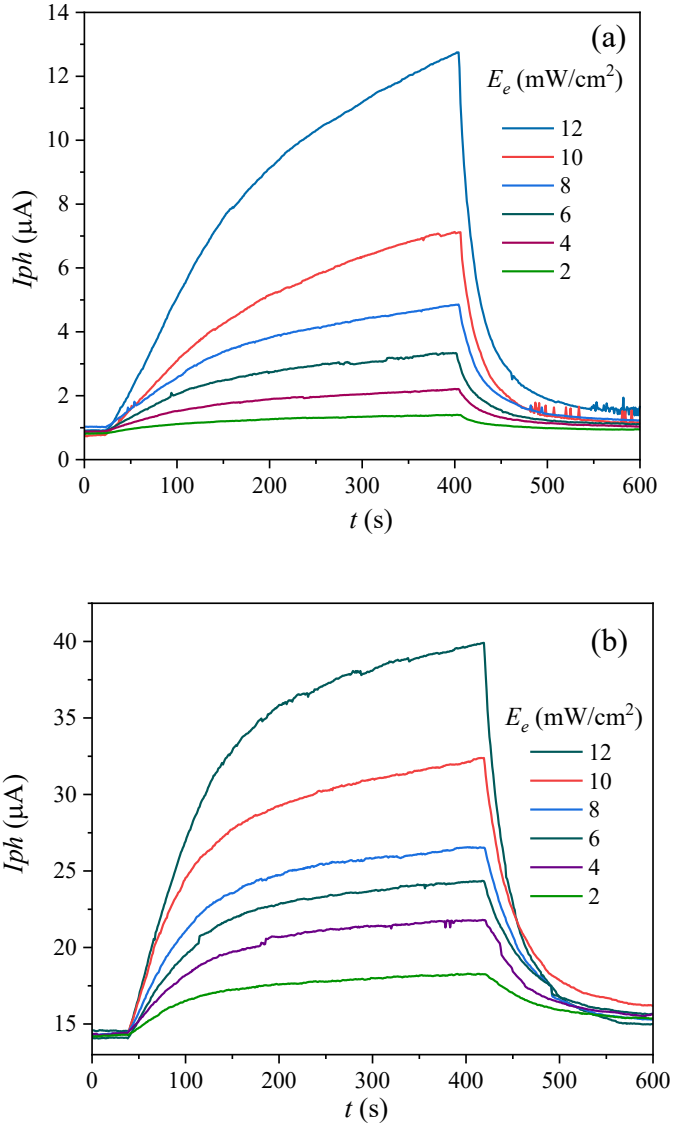
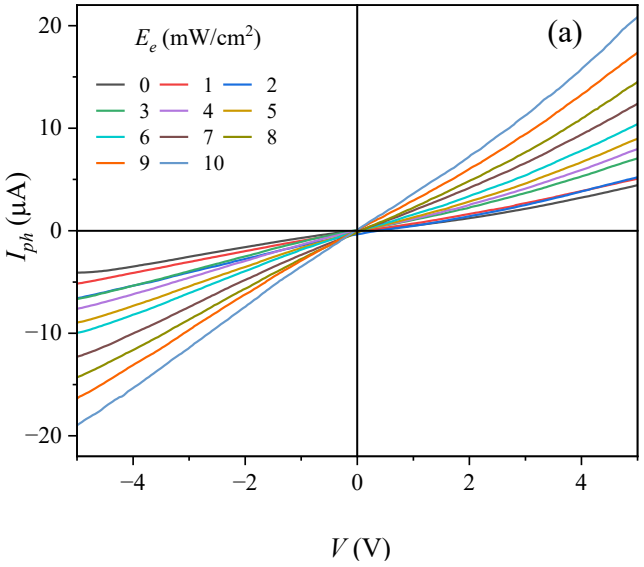


Figure 9


(a)
E_e (mW/cm^2)
0 1 2
3 4 5
6 7 8
9 10
I_{ph} (μA)
20
10
0
−10
−20
−4
−2
0
2
4
V (V)

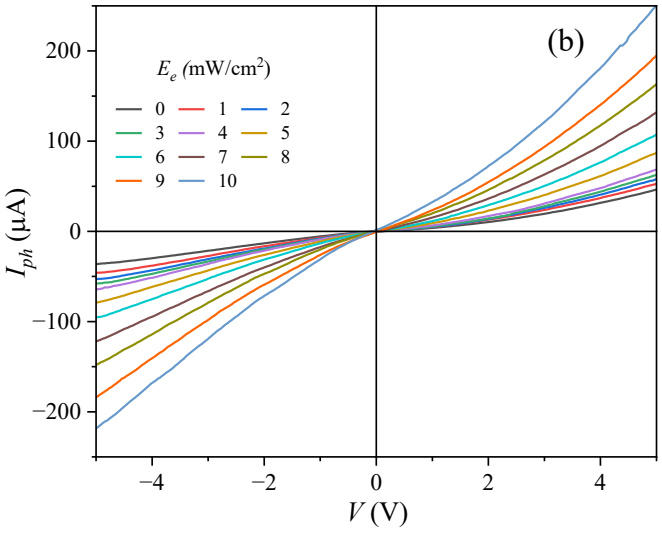

(b)
E_e (mW/cm^2)
0 1 2
3 4 5
6 7 8
9 10
I_{ph} (μA)
200
100
0
−100
−200
−4
−2
0
2
4
V (V)

Figure 10

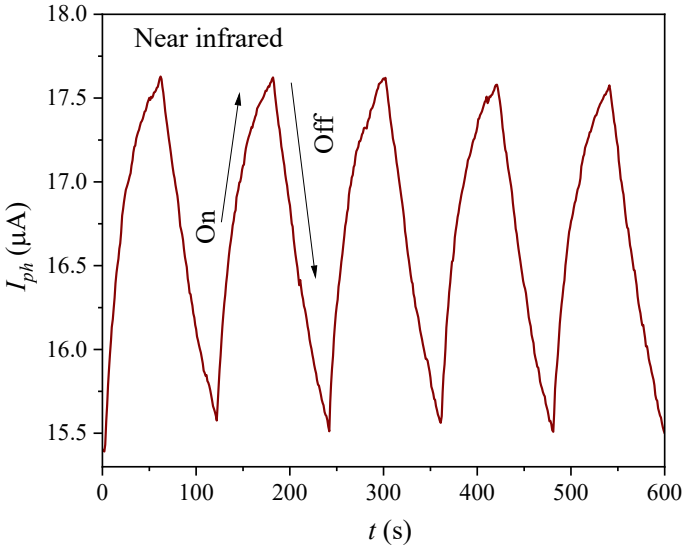
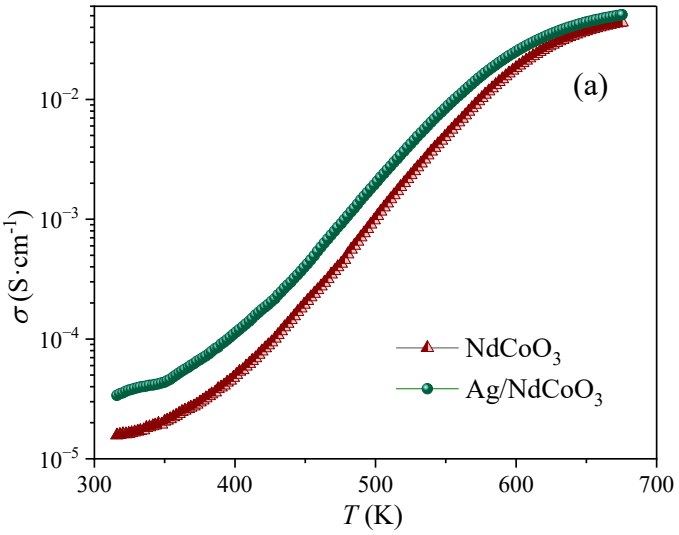

Near infrared
On
Off
I_{ph} (μA)
t (s)
18.0
17.5
17.0
16.5
16.0
15.5
0
100
200
300
400
500
600

Figure 11


(a)
10^{-2}
10^{-3}
10^{-4}
10^{-5}
σ (S·cm^{-1})
300
400
500
600
700
T (K)
NdCoO$_3$
Ag/NdCoO$_3$

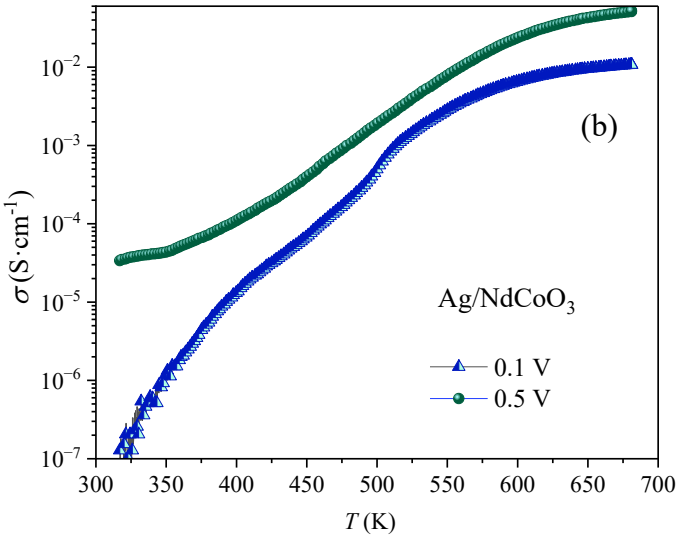

(b)
10^{-2}
10^{-3}
10^{-4}
10^{-5}
10^{-6}
10^{-7}
σ (S·cm^{-1})
300
350
400
450
500
550
600
650
700
T (K)
Ag/NdCoO$_3$
0.1 V
0.5 V

Figure 12

Table 1

Method	Reagents	Crystal Structure	Morphology/size	Calcination (°C)	Ref.
Coprecipitation	Nd, Co hydroxides, HNO_3	Cubic	Agglomerated NPs	900	14
Coprecipitation	$Co(CH_3CO_2)_2{\cdot}4H_2O$ $Nd(NO_3)_3{\cdot}6H_2O$, H_2O, C_2H_5OH	Cubic	μPs (100-400 nm)	800	15
Sol-gel	Nd, Co nitrates, H_2O, urea	Cubic	N/A	1100	16
Coprecipitation	$NdCl_3{\cdot}nH_2O$, $CoCl_2{\cdot}nH_2O$, H_2O	Orthorhombic	μPs (80-320 nm)	1000	17
Citrate	Nd, Co nitrates, citric acid	Orthorhombic	μPs (20-300 nm)	900	18
Thermal decomposition	$NdCl_3{\cdot}nH_2O$, $K_3[Co(CN)_6]$	Orthorhombic	N/A	922	19
Solid-state reaction	Nd_2O_3, $CoCO_3$	N/A	N/A	1127	20
Citrate	Nd, Co nitrates, EDTA	Cubic	Porous solid	1100	21
Solid-state reaction	Nd_2O_3, Co_3O_4	Orthorhombic	N/A	1200	22
Solid-state reaction	Nd_2O_3, Co_3O_4	Cubic	N/A	1000	23
Solid-state reaction	Nd_2O_3, Co_3O_4	Orthorhombic	Grain size > 5 μm	1100	24
Magnetron sputtering	Nd, Co	Orthorhombic	Films 500 nm thick	550	25
Salt-assisted combustion	Nd, Co nitrates, NaCl, glycine	Orthorhombic	Polyhedral NPs <200 nm	700	26
Molten salt	$NdCl_3{\cdot}6H_2O$, $CoCl_2{\cdot}6H_2O$, NaOH	Orthorhombic	Particles (0.5-20 μm)	1100	27
Glycolate sol-gel	Nd_2O_3, acetic acid, $Co(NO_3)_2{\cdot}6H_2O$,	Cubic	μPs (100-500 nm)	1000	28
Electrospinning	Nd nitrate, $CoAc{\cdot}4H_2O$, PVP, *N*, *N*-dimethylformamide	Orthorhombic	Fibers 256 nm diameter	700	29
Microwave-assisted combustion	Nd, Co nitrates, $AgNO_3$, H_2O, PVA	Cubic	μPs (120-300 nm)	-	This work

Table 2

E_e (W/m^2)	R_s ($\times 10^{-4}$ A/W)	
	$NdCoO_3$	$Ag/NdCoO_3$
20	12.4	98.7
40	16.6	95
60	20.3	84.7
80	25	77.6
100	32	92
120	50	109